

# A novel pulse shortcut strategy for simulating nano-second pulse electrochemical micro-machining

E. L. Hotoiu · J. Deconinck

Received: 6 July 2014 / Accepted: 3 September 2014 / Published online: 12 September 2014  
© Springer Science+Business Media Dordrecht 2014

**Abstract** Nano-second pulse electrochemical micro-machining is essentially employed in high precision metal processing applications. Simulation wise, such a process involves heavy time-accurate calculations necessary to obtain the confined anodic current density distribution, crucial for the machining copy accuracy. A new alternative simulation method is presented, entitled the Pulse Shortcut Strategy (PSS), that avoids the entire time-accurate procedure and significantly reduces the computational effort and runtime. The PSS relies on calculating a current density Correction Factor (CF) that is based on the local electrolyte resistance, the interface polarization and double layer (DL) properties in combination with the nano-second pulse characteristics. The same confining effect is achieved by simulating a computationally cheap stationary current density distribution and altering it locally through the space-dependent CF. When the system has constant electrolyte resistivity, constant DL capacitance and linear polarization, the CF calculation reacts in full agreement with the time-accurate simulation results for any pulse on-time/off-time combination. The PSS accuracy is compared with full time-accurate simulations and represents a mutual validation method between the two. These results offer promising perspectives for the simulation of nano-second pulse electrochemical micro-machining, making it more attractive from a practical point of view once the general interest in the technology emerges. The approach can be generalized to other pulsating electrochemical systems.

**Keywords** Nano-second pulse · Electrochemical micro-machining · Numerical simulations · Correction factor · Equivalent electric circuit

## 1 Introduction

Nano-second pulse electrochemical micro-machining (PECM) is a controlled anodic dissolution process for removing metal with high accuracy [8, 25]. The procedure is regularly employed in applications requiring an increased level of finesse, aiming to obtain high precision, superior surface quality parts, at smaller geometrical scales [2, 15, 23]. In contrast to conventional ECM, the electrodes are subjected to a lower amplitude pulse voltage (in the range of 1.5–10 V), instead of higher DC voltages. The use of ultrashort pulses (usually <100 ns) enhances the precision by confining the faradaic current density responsible for material removal, a few microns near the tool [12, 13, 25]. The confinement is due to the incomplete loading of the double layer (DL) in regions furthest from the tool, which receive a lower current density, in combination with the anodic dissolution reaction. To exploit this effect, the shape, length and amplitude of the applied pulses are crucial. Taking all these factors into account complicates the entire machining process significantly, both from the experimental and the simulation point of view.

In general, the pulse electrochemical machining (PECM) facilitates a systematic improvement of the limitations encountered in DC ECM. The pulse signal applied at the electrodes generates high instantaneous currents with sharp ripples, which are beneficial for the metal removal accuracy. As each pulse is followed by a longer off-time, the system relaxes and the material removal is performed intermittently. Inherently, the generated heat is less intense

E. L. Hotoiu (✉) · J. Deconinck  
Research Group Electrochemical and Surface Engineering, Vrije  
Universiteit Brussel, Pleinlaan 2, 1050 Brussels, Belgium  
e-mail: ehotoiu@gmail.com

and the by-products to be removed less consistent, allowing the use of a lower electrolyte flow velocity. The pulses combined with an efficient gap flushing helps the PECM to be conducted at smaller inter-electrode gaps (micrometres) which is a critical factor for improving the machining accuracy [16, 24, 27].

Significant progress has been published regarding research on the experimental side of the electrochemical micromachining (ECMM) [1, 7, 14, 19, 20, 25]. In the literature concerning numerical simulations, Deconinck [4–6] presented a detailed analysis of the DC ECM process, using the *Multi-ion Transport and Reaction Model*. Regarding PECMM, Kozak [17, 18]; Burkert [1]; Kenney and Hwang [10, 11] provided time-accurate computations for predicting the material dissolution rate.

Based on the *Finite Element Method* and using the *Potential Model* (PM) in combination with the DL capacitance and a non-linear reaction polarization, full time-accurate calculations have been performed in our previously published work [8]. The aim was to investigate the pulse detail level and to reveal how the pulse signal characteristics combined with the DL and the polarization influence the machining current density and finally the machined profile at low time scales.

However, the nano-second PECMM is a multi-time-scale problem and the simulation of the full time range of the process becomes extremely heavy when sub-nano-second time steps are required in the calculations. Significant efforts have been made to tackle such issues, yielding shortcut techniques such as the so-called *Time Averaging Method*. For instance, Smets [27–29] used the time averaging to perform temperature calculations in the context of PECM.

The method presented by Smets was adapted to serve the purposes of nano-second PECMM and enabled shape change and temperature calculations by creating a bridge between the very different ( $10^9$ ) time scales involved in the process. By using time averaging, the confining effects [8] occurring at the pulse detail level were transferred to the much higher time scale of the electrode deformation, as described in our earlier work [9]. Calculating the process over the full time range still requires considerable computational effort, even when employing the time averaging to link the time scales.

The present paper proposes an innovative method to cut short the calculations further, without losing any precision of the confining effects occurring at the pulse detail level. The new technique is based on the so-called *Pulse Shortcut Strategy* (PSS) and was designed to bypass the entire time-accurate/time-averaging calculation sequence. The strategy of avoiding the time-accurate pulse simulations relies on the idea that the initial pulse transient of the first few pulses

is insignificant compared to the large amount of nano-second pulses the process requires and essentially for which a quasi-steady-state pulsing regime can be assumed.

Based on a numerically determined *Correction Factor* (CF), the highly time-dependent nano-second PECMM process can be tackled through stationary simulations included in time-accurate shape change simulations working at much larger time steps. This solution dramatically reduces the computational effort and while remaining fairly accurate, it offers a viable solution that can be implemented into a commercial PECMM software.

The paper is structured as follows: First, it explains the method and the conditions under which the local CF can be calculated and further used to avoid time-accurate simulations at a nano-second pulse level. Then, the PSS approach based on the CF is applied and compared to full scale time-accurate calculations, under identical conditions.

To understand the context of the current work, referral to previous papers published by the authors on the nano-second PECMM topic is *essential* [8, 9]. The PSS should be regarded as an important theoretical contribution to the software tools currently employed to simulate ECM at nano scale. The theory behind the simulation tools that have been developed presents general validity that the electrochemical machining community can benefit.

## 2 Theory

### 2.1 Current density path analogy

The PSS mathematical formulation is built on the fact that any inter-electrode current density path can be seen as an electrical equivalent circuit. It is further assumed that there is proper electrolyte flushing such that the electrolyte conductivity remains sufficiently constant. For any geometrical configuration, the current density distribution along the electrodes can be calculated. When a potential difference of 1 V is applied, the local length of the current path to the opposed electrode can be calculated at any given place. The path is equal to the inverse of the local electric field as  $\Delta V = - \int_{\text{current line}} \mathbf{E} d\mathbf{l} = \|E\| \int_{\text{current line}} d\mathbf{l} = \|E\| l_{\text{current line}}$  such that for a 1 V applied potential  $\Delta V = \rho l J = 1 \rightarrow E = 1/l$ .

In the electrochemical cell, the electrolyte is assumed to behave as a resistor meaning that the geometry and conductivity are constant, at least at the nano-second pulse level. Although the electrode reactions and DL are very complex entities [22], the proposed model assumes that they can be described by discrete components. So, the interfaces can be seen as parallel circuits representing the polarization resistances  $R_a$ ,  $R_c$  and the DL capacitances  $C_a$ ,

**Fig. 1** The equivalent RC electric circuit of a current density path. **a** includes both interfaces, polarized anodically and cathodically. **b** includes the anodic polarized interface. **c** includes the anodic non-polarized interface

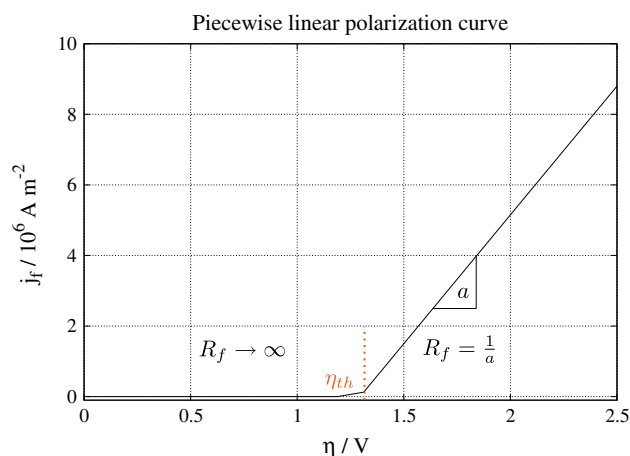
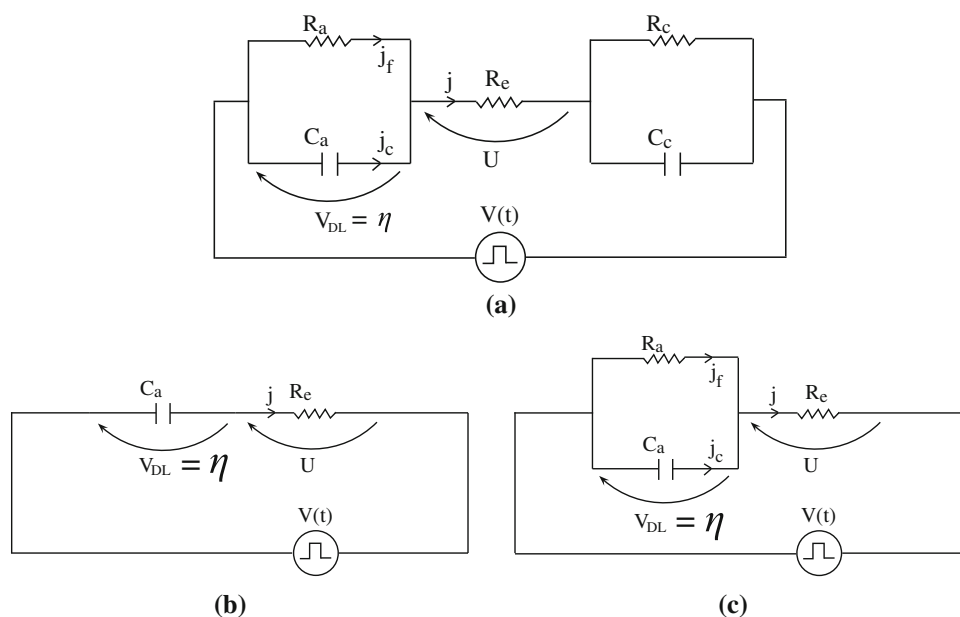


**Fig. 2** Piece-wise linear polarization curve reflecting the interface reaction measured behavior.  $\eta_{th}$  is the onset overpotential threshold for which the corresponding current density is zero

$C_c$  at the two interfaces. It is further assumed that the DL capacitances are constant. Connecting the interfaces in series with the electrolyte resistance and the pulse source yields the equivalent circuit of the current density line inside the cell, as depicted in Fig. 1a.

In the given context, interest is focused on the anodic interface, the equivalent circuit of the current density line can be simplified further by dropping the cathodic component (without any loss of generality).

The anodic polarization at high current densities is a combined effect of a metal dissolution reaction and the formation of a so-called jelly layer that involves a mass transfer process. Several experimental observations reveal a very low current density below a threshold potential

followed by a linear behavior at larger overpotentials [2–4, 21, 26]. In agreement with these measurements, such a linearised anodic polarization curve has been chosen in this work. The faradaic current density, related to the electrochemical reactions, is driven by the overpotential  $\eta = V - U - E_0$ , still remaining general, the cell equilibrium potential  $E_0$  at zero current can be omitted here.

As illustrated in Fig. 2, a mathematical piece-wise linear function approximating such an onset linear polarization behavior is further employed. The overpotential threshold value  $\eta_{th}$  (V) delimits the polarization onset, corresponding to the current density zero level or an infinite  $R_f$  resistance. Beyond the threshold, the current density increases linearly and the polarization is characterized by a reaction resistance inversely proportional to the slope  $a$ . Therefore, the polarization region where  $\eta \leq \eta_{th}$  corresponds to the circuit given in Fig. 1b while for  $\eta > \eta_{th}$ , the equivalence shifts to the circuit provided in Fig. 1c.

Considering a constant DL capacitance and a piece-wise linear polarization, assumptions of paramount importance within the current model and supposing that the electrolyte behaves largely linear along a current line, for any given geometrical configuration, the two circuit phases 1b and 1c are described by their specific differential equations, given in Eq. 1 as

$$\begin{cases} \frac{d\eta(t)}{dt} + \underbrace{\frac{1}{CR_e}}_{1/\tau_1} \eta(t) = \frac{V(t)}{CR_e}, & \eta \leq \eta_{th} \\ \frac{d\eta(t)}{dt} + \underbrace{\left(\frac{1}{CR_f} + \frac{1}{CR_e}\right)}_{1/\tau_2} \eta(t) = \frac{V(t)}{CR_e}, & \eta > \eta_{th} \end{cases}, \quad (1)$$

where  $\eta$  (V) represents the potential drop (overpotential) across the DL,  $C = C_a$  (F) is the anodic DL capacitance and  $V(t)$  (V) is the pulsed potential applied at the electrodes. The two circuits yield their distinct time constants, denoted  $\tau_1$  and  $\tau_2$  (s), respectively.

The explicit analytical solution of the two equations is not essential but it supports the development of the PSS theory and is the starting point of the present work.

The circuit parameters need to be expressed per unit surface  $S$ , for practical use. Therefore, the electrolyte resistance  $R_e$  becomes

$$R_e = \frac{l}{\kappa S} = \frac{l}{\kappa} \quad (2)$$

and is directly proportional to the inter-electrode gap  $l$  (m) along a current density line and inversely proportional to the electrolyte electrical conductivity  $\kappa$  ( $\text{S m}^{-1}$ ).

The non-linear faradaic resistance  $R_f$  takes the following expression

$$R_f = \begin{cases} \infty, & \eta \leq \eta_{th} \\ \frac{1}{aS} = \frac{1}{a}, & \eta > \eta_{th} \end{cases}, \quad (3)$$

where  $a$  ( $\text{S m}^{-2}$ ) is the slope of the linear interface polarization curve. The link between the resistance  $R_f$  and the linear polarization is visualized in Fig. 2.

Finally, the DL capacitance becomes

$$C = \frac{\epsilon}{d} S = \frac{\epsilon}{d}, \quad (4)$$

with  $\epsilon/d$  ( $\text{F m}^{-2}$ ) the specific DL capacitance, where  $\epsilon$  ( $\text{F m}^{-1}$ ) is the electrical permittivity of the medium and  $d$  (m) is the DL thickness.

Based on the specific circuit parameters, the time constants of the two systems can be written as

$$R_{eq}C = \begin{cases} \tau_1 = \frac{\epsilon l}{d\kappa}, & \eta \leq \eta_{th} \\ \tau_2 = \frac{\epsilon l}{d(\kappa + al)}, & \eta > \eta_{th} \end{cases}, \quad (5)$$

where  $R_{eq}$  ( $\Omega$ ) is the corresponding equivalent resistance for the two circuits.

## 2.2 Quasi-steady-state system response

When the electrodes are subjected to a nano-second pulse signal, the nano-second transient response is almost insignificant when compared to the total processing time such that it can be assumed that the process functions in pulsed steady-state conditions. This means that the steady-state system response can be calculated locally, at any electrode position, in an analytical way. The relevant quantity

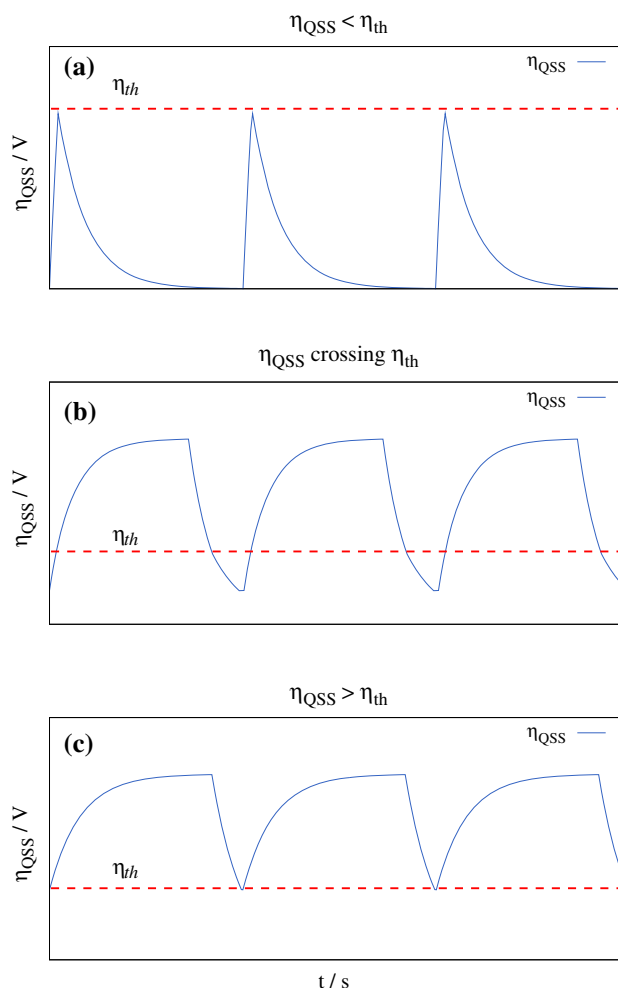


**Fig. 3** The relevant QSS overpotential situations with respect to the threshold  $\eta_{th}$ , depending on the applied pulses. **a**  $\eta_{QSS} < \eta_{th}$ . **b**  $\eta_{QSS}$  is below and above  $\eta_{th}$ . **c**  $\eta_{QSS} > \eta_{th}$

becomes the time-dependent overpotential  $\eta_{QSS}(t)$  that can be determined for the different polarization phases.

Depending on the amplitude and the pulse-to-pause ratio of the applied pulses, the response  $\eta_{QSS}$  can be situated in one of the three scenarios given in Fig. 3. While in the first case the faradaic reaction is never triggered due to insufficient  $V_{on}$  or  $t_{on}$ , in the last situation the DL does not unload below the threshold  $\eta_{th}$  value, thus the system never relaxes sufficiently due to a large  $V_{on}$  and small  $t_{off}$ . The insufficiency can be explained by the fact that the DL loads up faster than the optimal time, allowing too much energy into the parallel faradaic reaction and yielding a more diffuse current density that damages the overall machining accuracy [8]. The intermediate scenario, depicted in Fig. 3b, is the only general and relevant one from a practical point of view, allowing an intermittent applied current density which is most beneficial for the machining precision.

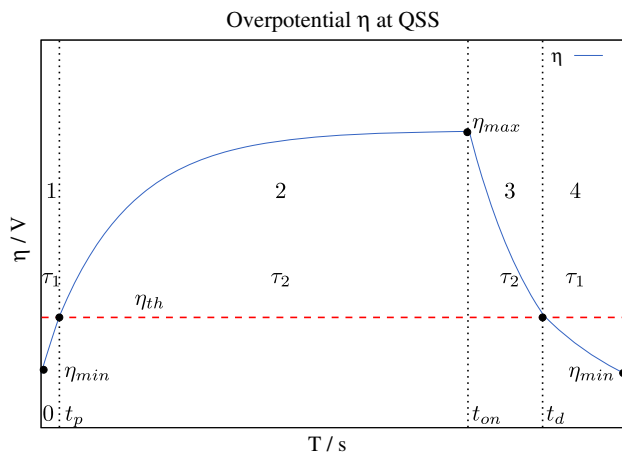


**Fig. 4** QSS overpotential for one time period  $T$ . The piece-wise linear polarization divides the DL overpotential in four phases during the loading/unloading cycle

When looking at a single QSS pulse, with respect to the onset linear polarization, four phases can be identified as is indicated in Fig. 4. The four phases representing the DL loading/unloading cycle are described by the two RC configurations in Fig. 1b (phase 1 and 4) and Fig. 1c (phase 2 and 3). Phases 1 and 4 have the time constant  $\tau_1$  while phases 2 and 3 share the same  $\tau_2$ . The pulse period  $T$  is divided to four distinct times,  $t_p$ ,  $t_{on} - t_p$ ,  $t_d - t_{on}$  and  $T - t_d$ , where  $t_p$  is the time required to reach the polarization threshold  $\eta_{th}$  when the DL loads,  $t_{on}$  is the applied pulse on-time and  $t_d$  is the time required to depolarize to the threshold  $\eta_{th}$  when the DL unloads.

Defining the DL overpotential at QSS implies knowing the overpotential minimum value  $\eta_{min}$ , the loading time  $t_p$ , the overpotential peak  $\eta_{max}$  and the unloading time  $t_d$ . Being at steady state, the starting  $\eta_{min}$  is equal to the ending value over a time period  $T$ . To calculate the aforementioned parameters, the following system of equations needs to be solved numerically.

$$\begin{cases} \eta_{th} = \eta_{min} e^{-\frac{t_p}{\tau_1}} + V_{on} \left(1 - e^{-\frac{t_p}{\tau_1}}\right) \\ \eta_{max} = \eta_{th} e^{-\frac{t_{on}-t_p}{\tau_2}} + \frac{\kappa}{\kappa + al} V_{on} \left(1 - e^{-\frac{t_{on}-t_p}{\tau_2}}\right) \\ \eta_{th} = \eta_{max} e^{-\frac{t_d-t_{on}}{\tau_2}} \\ \eta_{min} = \eta_{th} e^{-\frac{T-t_d}{\tau_1}} \end{cases}, \quad (6)$$

In Eq. 6,  $\tau_1$  and  $\tau_2$  are space-dependent and different for any inter-electrode current path length  $l$ .

After applying a pulse signal, pre-calculating the four unknowns (marked in red) is possible for a given range of inter-electrode path lengths  $l$ . Having the four parameters describing the QSS overpotential, the mathematical

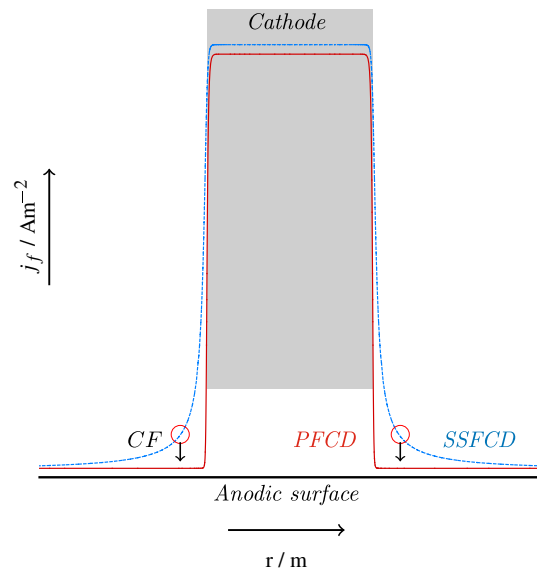


**Fig. 5** Generic comparison between a confined (PFCD) and a spread steady-state (SSFCD) faradaic current density distribution

expression for  $\eta_{QSS}$ , over one QSS time period  $T$ , can be introduced as

$$\eta_{QSS} = \begin{cases} \eta_{min} + (V_{on} - \eta_{min}) \left(1 - e^{-\frac{t}{\tau_1}}\right), & t \in [0, t_p] \\ \eta_{max} \left(1 - e^{-\frac{t-t_p}{\tau_2}}\right), & t \in (t_p, t_{on}] \\ \eta_{max} e^{-\frac{t-t_{on}}{\tau_2}}, & t \in (t_{on}, t_d] \\ \eta_{th} e^{-\frac{t-t_d}{\tau_1}}, & t \in (t_d, T] \end{cases}, \quad (7)$$

where  $t_p$ ,  $\eta_{min}$ ,  $\eta_{max}$  and  $t_d$  are now known, together with the other system parameters: the electrolyte conductivity  $\kappa$ , polarization slope  $a$  and onset  $\eta_{th}$ , the pulse  $t_{on}$  and period  $T$  and the time constants  $\tau_1$  and  $\tau_2$ .

The system in Eq. 7 fully characterizes the QSS overpotential in Fig. 4.

### 2.3 Current density correction factor

The entire PSS relies on the so-called current density CF. A visual description of the concept of a local CF, applied to a current density distribution, is given in Fig. 5. A computationally cheap, non-confined steady-state faradaic current density (SSFCD) distribution is transformed into a confined distribution (PFCD), specific for a time-accurate pulse simulation.

The CF alters the SSFCD in every spatial point along the anodic surface, aligning it to the PFCD, without needing extremely expensive time-accurate simulations. The CF

formulation proposes a novel strategy to bypass the expensive time-accurate calculations, while keeping the pulse confining properties over the current density distribution.

The CF in any point located on the anodic surface, corresponding to a given current density path line, can be expressed by a ratio between the time averaged QSS PFCD and the SSFCD in that point and is equal to

$$CF(\mathbf{r}) = \frac{\frac{1}{T} \int_0^T j_f(\mathbf{r}, t) dt}{j_{fss}(\mathbf{r})} = \frac{\frac{1}{T} \int_0^T a \eta_{QSS}(t) dt}{j_{fss}(\mathbf{r})}, \quad (8)$$

where the PFCD is  $j_f(t) = a \eta_{QSS}(t)$  and  $a$  is the polarization slope.

The steady-state faradaic current density  $j_{fss}$  (SSFCD), is a non-pulsed current density whose distribution can be obtained by a stationary simulation. In fact, this is the distribution that has to be corrected by CF, with the aim to obtain similar confinement of the pulsed faradaic current density distribution  $j_f(t)$  (PFCD). Therefore,  $j_{fss}$  is the steady-state local secondary current density scaled with the pulse on-time

$$j_{fss} = \frac{a\kappa}{\kappa + al} V_{on} \frac{t_{on}}{T}. \quad (9)$$

Having defined  $\eta_{QSS}(t)$  in Eq. 7, based on the onset linear polarization configuration and after integration, the CF can explicitly written as

$$CF = \begin{cases} 0, & \eta_{QSS} \leq \eta_{th} \\ \frac{a \cdot \eta_{max}}{T \cdot j_{fss}} \left[ \left( e^{-\frac{t_{on}-t_p}{\tau_2}} - e^{-\frac{t_d-t_{on}}{\tau_2}} \right) \tau_2 + t_{on} - t_p \right], & \eta_{QSS} > \eta_{th} \end{cases}. \quad (10)$$

As a verification of Eq. 10, consider for instance that  $t_{on}$  is very long such that  $t_{on} \rightarrow \infty$ . As a consequence  $CF \rightarrow 1$  and the current density distribution aligns to the spread SSFCD.

The CF behavior and its direct application will be further explained in the results Sect. 4, using concrete input data.

#### 2.4 Correction factor integration principle

The PSS is defined as a combination of the previously described CF and the PM addressed in a previous publication concerning the nano-second pulse  $\mu$ ECM simulations [8].

In a 2D/3D electrochemical system, by applying a DC voltage signal and associated polarization at the electrodes, the SSFCD distribution  $\mathbf{j}_{fss}$  (Fig. 5), normal to the anodic surface, can be obtained by numerically solving the following stationary charge conservation equation

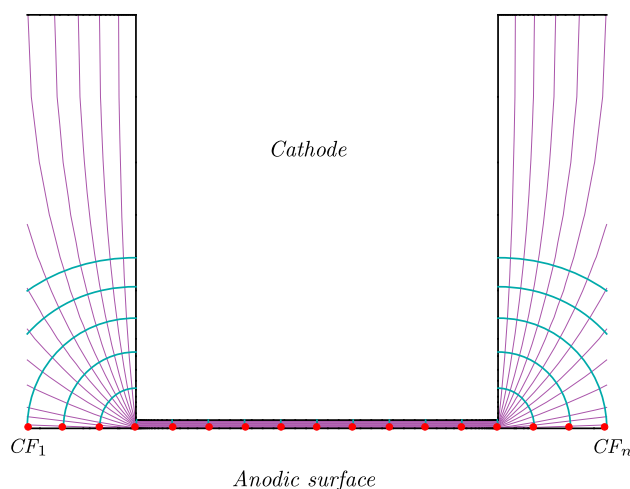


**Fig. 6** Local current density paths based on the potential distribution in the inter-electrode gap. The red dots mark generically few anodic spots where the local current density is corrected based on the CF

$$\nabla \cdot \mathbf{j}_{fss} = \nabla \cdot (\kappa \nabla U) = 0, \quad (11)$$

yielding  $\mathbf{j}_{fss}$  as a flux

$$\mathbf{j}_{fss} = -(\kappa \nabla U) \cdot \mathbf{1}_n, \quad (12)$$

where  $\kappa$  ( $S m^{-2}$ ) is the electrolyte conductivity,  $U$  (V) is the electrolyte potential distribution and  $\mathbf{1}_n$  (m) the unit vector normal to the surface.

By calculating a primary current density distribution in advance, the resistance of all the current density paths yield a resistance distribution in between the electrodes. As explained, the length  $l$  of the current path between a point on an electrode and the counter electrode equals

$$l = \kappa \cdot \frac{U}{j_{fss}}. \quad (13)$$

Having found the range of inter-electrode distances  $l$  and knowing all the electrochemical properties (the electrolyte conductivity  $\kappa$ , the piece-wise linear polarization with the slope  $a$  and the DL specific capacitance  $\epsilon/d$ ) for any desired pulse parameters  $V_{on}$ ,  $t_{on}$  and  $T$ , the CF given in Eq. 10 can be obtained.

Therefore, the confining effect (realized by the pulses in combination with the DL capacitance and changing polarization resistance) on the current density passing the anodic interface can be applied locally through the CF, as is visualized in Fig. 6.

In Fig. 6, a few generic anodic correction points are marked in red for visual understanding. Solving the stationary PM results in a SSFCD along the anodic surface which is then corrected locally (in any anodic point) based on the expression



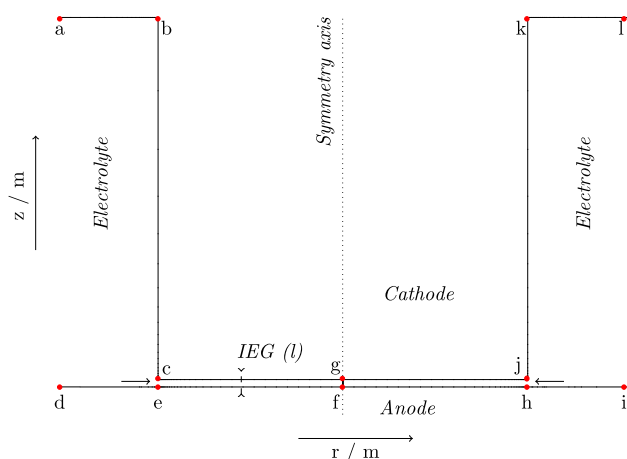


**Fig. 7** Axisymmetric schematic of the electrochemical cell for nano-second pulse  $\mu$ ECM. Relevant points are marked for further use in the text

$$j_{f_n} = CF \cdot j_{f_{ssn}}, \quad (14)$$

where  $n$  is the index of a point on the surface, and yields the confined current density distribution profile (PFCD) as indicated in Fig. 5.

The way the PSS works in practice will be analysed and discussed further.

### 3 Simulation prerequisites

#### 3.1 Geometry and numerical discretization

The electrochemical cell used in the simulations is a typical set-up employed to machine a micro hole in a flat plate, having an axisymmetrical geometry as generically shown in Fig. 7. Only the right-hand side is considered for symmetry reasons. The cathode (tool) is a small cylindrical rod of radius  $\|gj\| = 50 \mu\text{m}$  and height  $\|jk\| = 100 \mu\text{m}$ , having the side wall  $\|jk\|$  active or passive. On the opposite side, is the initially flat anode (workpiece) with a radius  $\|fi\| = 500 \mu\text{m}$ . The tool and the anode workpiece are separated by a very narrow channel gap filled with the electrolyte solution.

Throughout the simulations, the tool's radius  $\|gj\|$ , its height  $\|jk\|$  and the workpiece's radius  $\|fi\|$  are kept constant. The inter-electrode gap (IEG) used in the current simulations is  $\|gf\| = 2 \mu\text{m}$ .

Prior to performing numerical simulations using the *Finite Element Method*, the previously described geometry is discretized using linear triangular elements as illustrated in Fig. 8. The governing equations, described in Sect. 2.4, are solved yielding the potential in every node.

The simulation mesh illustrated in Fig. 8 contains approximately 2,600 nodes. The discretization is much

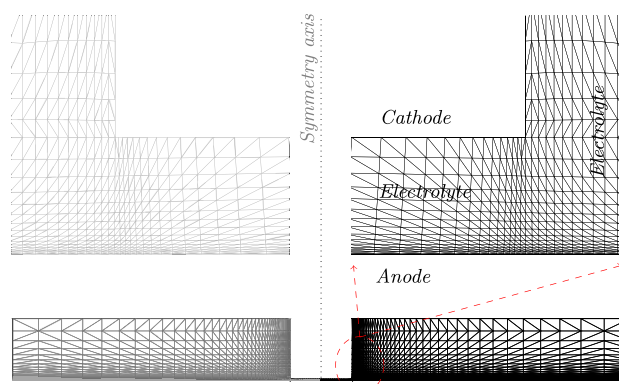


**Fig. 8** A typical computational axisymmetric geometry (down right) having approximately 2,600 nodes containing boundary layers with a thickness of 10 nm. For better observation a zoom-in (up right) of the thin channel is provided

finer around the gap (typical element dimension of 10 nm) and sufficiently fine throughout the rest of the domain to ensure mesh-independent results. At the electrolyte-electrode interfaces, dense boundary layers are used to account for any steep gradients present in the solution field. Away from the tool, the mesh is much coarser.

#### 3.2 Simulation parameters

The relevant parameters in the current context are related to the interface polarization, the DL capacitance, the pulse characteristics and the geometrical specifications treated in Sect. 3.1.

An essential condition for the PSS well-functioning and the current density confinement in general is imposed by the considered reaction polarization, as already discussed in Sect. 2. The piece-wise linear curve depicted in Fig. 2 will be further employed, having a slope  $a = 3 \times 10^6 \text{ S m}^{-2}$  and an onset overpotential  $\eta_{th} = 1.3 \text{ V}$  [4]. Furthermore, it has been assumed that solely the anodic interface is polarized. The specific capacitance of the DL present at the workpiece-electrolyte interface was considered  $\epsilon/d = 0.1 \text{ F m}^{-2}$  and the constant electrolyte conductivity  $\kappa = 13.4 \text{ S m}^{-1}$ .

For this application, the pulses were imposed along the anodic boundary  $\|fi\|$ , having an amplitude of  $V_{on} = 5 \text{ V}$  with  $t_{on} = 100 \text{ ns}$  and the period  $T = 190 \text{ s}$ , if not mentioned otherwise. The cathodic contour  $\|gjk\|$  was set at zero potential. The chosen pulse on-time/off-time values are in approximative agreement with the DL loading/unloading times.

According to Sect. 3.1, the spacing between the electrodes, under the cathode, reads  $l = 2 \mu\text{m}$  and remains fixed as no anodic shape change in time needs to be considered during the nano-pulse sequence being looked at.

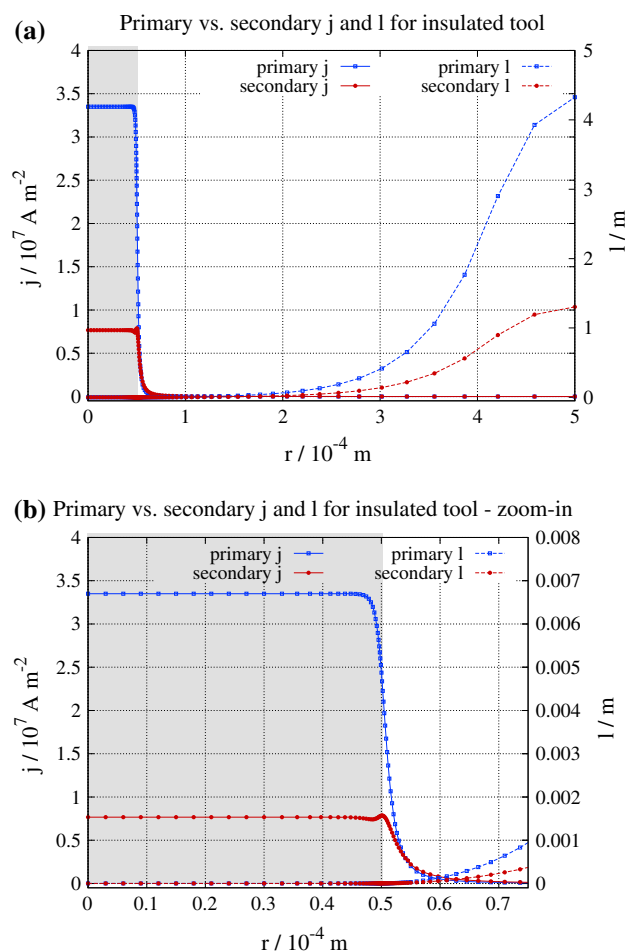


**Fig. 9** Stationary simulation of the primary versus secondary current density distribution  $j$  (left Y-axis) and calculated current path length  $l$  (right Y-axis) along the anodic radius. The grey rectangle marks the tool limits. The tool sidewalls were considered insulated. **a** entire radius. **b** zoom-in at the interest radius zone  $[0.5-0.6] \times 10^{-4}$  m where the current density confinement occurs

## 4 Results and discussion

### 4.1 Path length behavior

As the PSS relies on the locally calculated current path length in between the electrodes, a preliminary discussion on its behavior will reveal relevant information regarding the generality of the method. A series of numerical simulations is executed to study the influence of the interface properties on the path length, for both insulated and active tool sidewalls. Indeed, although the electrolyte acts as a constant resistor, one might expect that the polarization influences the inter-electrode length  $l$ .

A first set of stationary simulations reveals the difference between the calculated length  $l$  along the anodic surface based on a primary versus a secondary current density distribution. The employed onset polarization to

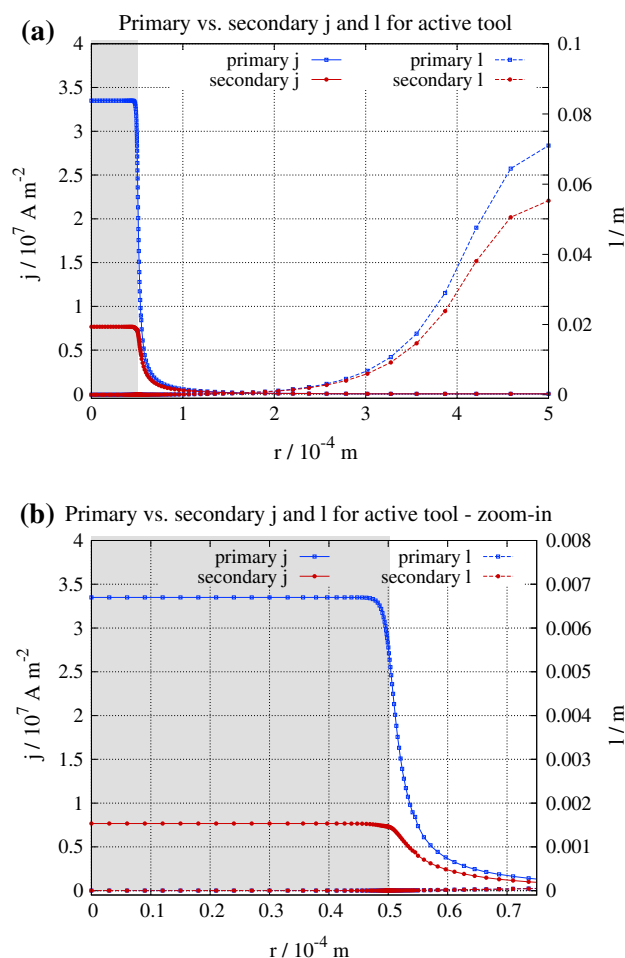


**Fig. 10** Stationary simulation of the primary versus secondary current density distribution  $j$  (left Y-axis) and current path length  $l$  (right Y-axis) along the anodic radius. The grey rectangle marks the tool limits. The tool sidewalls were considered active. **a** entire radius. **b** zoom-in at the interest radius zone  $[0.5-0.6] \times 10^{-4}$  m where the current density confinement occurs

obtain the secondary length distribution had the slope  $a$  and threshold  $\eta_{th}$ , as previously mentioned in the parameters section.

Figure 9a shows a comparison between the primary versus secondary current density distribution (left Y-axis), over the full radial dimension  $r$ , for insulated tool sidewalls. Based on the two current densities, the corresponding calculated lengths  $l$  are plotted on the right Y-axis. Despite the fact that at large radii the primary and the secondary lengths  $l$  are different, a zoom-in Fig. 9b at the confinement zone reveals that the deviation is minimal in this region, yielding the same confinement in the CF. The current density confinement, necessary for enhancing the metal removal precision occurs at radius values in the range  $[0.5-0.6] \times 10^{-4}$  m. In other words, using either a primary or a secondary current density distribution to calculate the length  $l$  essentially produces the same final result.



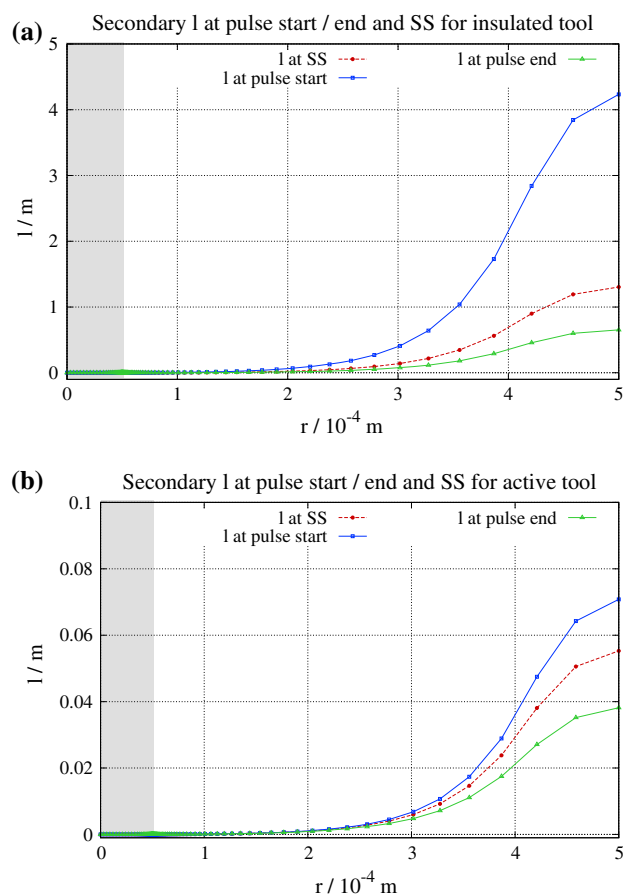


**Fig. 11** Time-accurate simulation of the current path length  $l$  for a secondary distribution. The calculated lengths at pulse start/end are compared to the stationary secondary steady-state length, which is always situated in between. The grey rectangle marks the tool limits. **a** For insulated tool sidewalls. **b** For active tool sidewalls

Figure 10a depicts the identical situation but now with active tool sidewalls, involving a current density distribution that is obviously more spread, away from the tool. However, the difference of the current density distribution outside the gap is not so pronounced when compared with Fig. 9a. This is because the narrow gap involves a large current density in the gap compared to outside where in both cases the distance between both electrodes increases fast.

Similar to the previous case (Fig. 9), the deviation impact is minimal in the final outcome as the two calculated lengths align well right up to higher radius values ( $r = 3 \times 10^{-4}$  m).

A second set of time-accurate numerical simulations explains the influence of the DL loading on the calculated current path length  $l$ . By applying a sufficiently long pulse, the length  $l$  is calculated at the beginning of the signal and then at the end. Figure 11 compares it to the steady-state length determined in stationary conditions.

For insulated tool sidewalls, the length at the pulse start is the same as the primary length, as expected. The observation

can be verified by comparing Fig. 11a with Fig. 9a. Note in Fig. 11a that the steady-state length is situated in an intermediate state between  $l$  at pulse start and pulse end, representing an average value. Moreover, all lengths are well aligned up to  $r = 2 \times 10^{-4}$  m, meaning that there is practically no difference between the three situations in the relevant confinement zone at  $r = [0.5–0.6] \times 10^{-4}$  m (tool projection marked with a grey rectangle). It is, therefore, safe to assume that the DL loading and polarization have no significant effect on the path length in the region of importance. By using either a primary or a secondary steady state  $l$ , the CF will essentially display identical behavior.

The same can be stated concerning the similar situation with active tool sidewalls. As Fig. 11b illustrates, the stationary steady-state length is intermediary (average) to the lengths at pulse start and pulse end. The deviation at large radius values is lower here as the lengths are also substantially shorter compared to the insulated case and in the relevant region, the three curves keep aligning beyond radius values of  $r = 2 \times 10^{-4}$  m.

The third and the final set of numerical simulations (stationary) presented in this section, reveals the influence of the polarization, with constant  $\eta_{th} = 1.3$  V, on the computed path length. As mentioned in Sect. 3.2, the applied potential is 5 V. The calculated lengths based on primary and three different secondary current density distributions are presented in Fig. 12a. Again, differences occur only at low current densities where an erroneous CF has no impact. When the tool is active the deviations further reduce, as can be seen in Fig. 12b. Further, a comparison between the reference onset polarization (green curve) and a plain linear polarization ( $\eta_{th} = 0$ , black marker curve) is presented showing no difference.

All calculations presented in this preliminary analysis show that current path lengths based on a primary or a secondary current density distribution are identical and sufficiently constant for practical use of the PSS, regardless if the tool is insulated or active. The electrolyte solution with constant conductivity essentially acts as a constant resistor that is insignificantly influenced by interface polarization or the DL loading in the confinement area. It is believed that this is due to the low polarization resistance. The onset potential does not influence this behavior. This is because (1) below  $\eta_{th}$  the current density is zero and (2) even when the current density is very small, it is still at overpotentials above  $\eta_{th}$ .

The deviations at very low current densities are possibly due to numerical rounding off errors as the grid is much coarser there and as the calculated length is proportional to the inverse of the current density. The latter generates important errors in  $l$  when the current density becomes irrelevantly small.

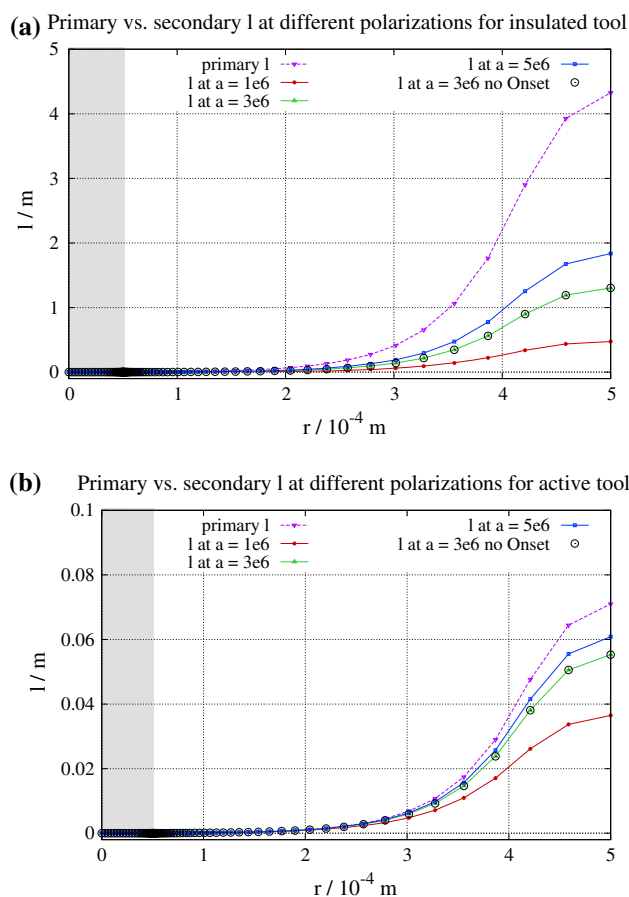


**Fig. 12** Stationary simulation of the secondary path length at different polarization slopes ( $a = 3e \text{ S m}^{-2}$  is the reference slope used across this work). A comparison with the primary length and with a plain linear polarization ( $\eta_{\text{th}} = 0$ ) is provided. The grey rectangle marks the tool limits. The tool sidewalls were considered insulated (a) and active (b)

## 4.2 Correction factor behavior

Besides its spatial dependency, the CF calculated in Sect. 2.3 is influenced by various conditions such as pulse, polarization and DL characteristics.

Using the parameters given in Sect. 3.2, for several applied pulse conditions, Fig. 13 shows the CF behavior when the inter-electrode current path length  $l$  increases. The pulse characteristics were chosen such that a concluding trend could be presented, ranging from low to high on- and off-times.

The CF can only take values between  $[0, 1]$ . Applying pulses with a shorter on-time confines the CF to short inter-electrode lengths  $l$ , at the cost of a reduced amplitude. For any pulse length, there is a corresponding critical gap  $l$  beyond which  $\text{CF} = 0$ . Then, the CF forces the current density distribution to zero, improving the confinement

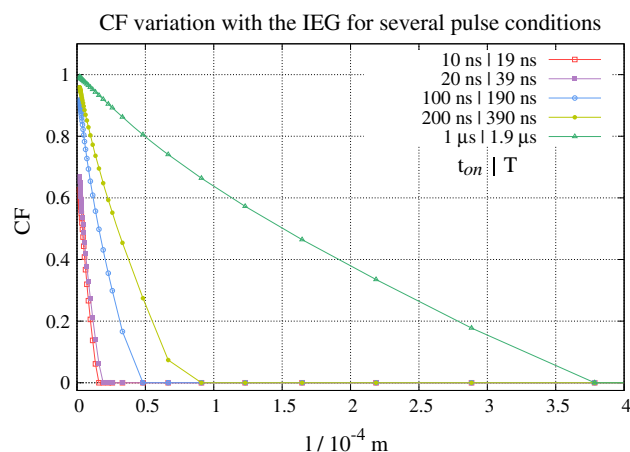


**Fig. 13** Pulse shortcut correction factor variation with the current path length, for several applied pulse conditions. The legend gives the pulse  $t_{\text{on}}$  and its period  $T$  in the format  $t_{\text{on}} | T$ . Independent of tool sidewall insulation

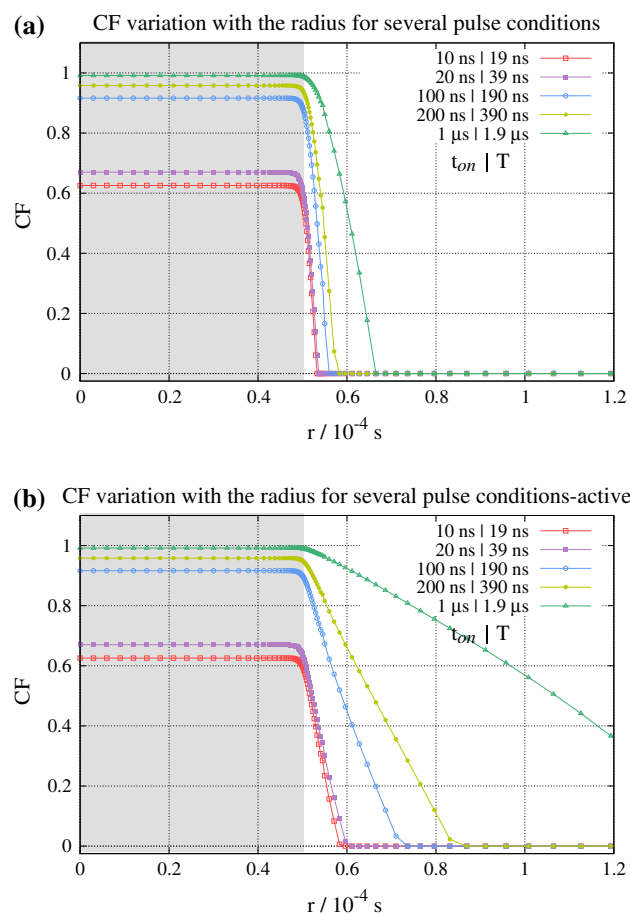


**Fig. 14** Pulse shortcut correction factor along the anodic radius, for several applied pulse conditions. The legend format is  $t_{\text{on}} | T$ . The grey rectangle marks the cathode limits. The tool sidewalls are insulated (a) and active (b)

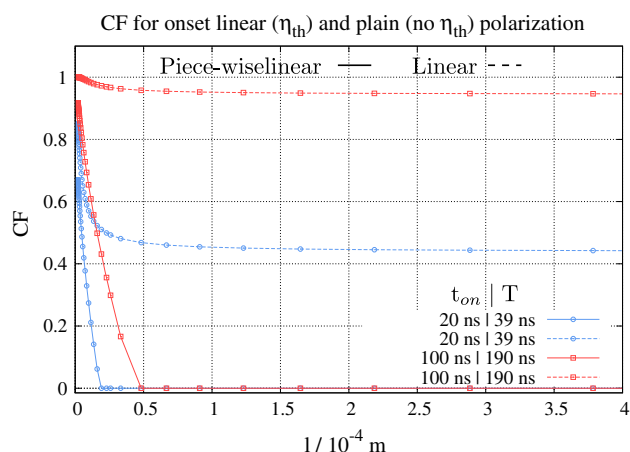


**Fig. 15** Pulse shortcut correction factor variation with the IEG for two distinct applied pulses. Comparison between the CF for a linear polarization with and without threshold potential  $\eta_{th}$ . Independent of tool sidewall insulation

locally. With shorter pulse on-times, the confinement is restricted to the immediate vicinity of the cathode.

On the other hand, if  $CF = 1$ , there is no correction. For example, if pulses with  $t_{on} = 1 \mu s$  are used, the CF decreases slowly, preserving values closer to *one*, even at large lengths  $l$ , such that the localization effect is lost in the vicinity of the tool.

Clearly, the CF acts similar to the full time-accurate pulsed simulations [8], where shorter on-times enhance the confinement while lower current density amplitudes are achieved.

A different perspective for Fig. 13 is given in Fig. 14, indicating the corresponding CF behavior along the anodic radius  $r$ , for the same pulse conditions. As the calculated inter-electrode gap is different for insulated or active sidewalls, the CF is also different and remains for longer non-zero in the latter case. Only by applying short nano-second pulses, the CF shows lower amplitudes while better confinement is achieved. In case of an insulating sidewall the CF drops faster to 0 but with sufficiently small pulses an active wall is also performing very good and less complicated in use.

The threshold potential  $\eta_{th}$  is absolutely necessary to obtain a significant confinement, in other words to obtain a CF that tends to zero as the distance  $l$  increases. This is shown in Fig. 15 in which two different pulses, with shorter and longer on-times, were chosen for an onset piece-wise linear ( $\eta_{th} > 0$ ) and a plain linear ( $\eta_{th} = 0$ ) polarization curve. Note how for both pulses, when  $\eta_{th}$  is *non-zero*, the CF suddenly becomes *zero* at relatively small current path lengths  $l$ . When  $\eta_{th}$  is *zero*, even at a very short pulse on-time, the CF does not drop to *zero* for any distance. Incrementing the on-time, the CF value increases for all lengths  $l$  and tends to *one* for longer pulse  $t_{on}$ . This role of the polarization on the

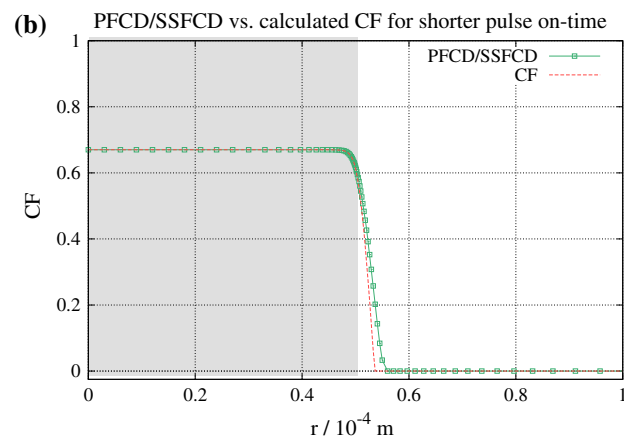
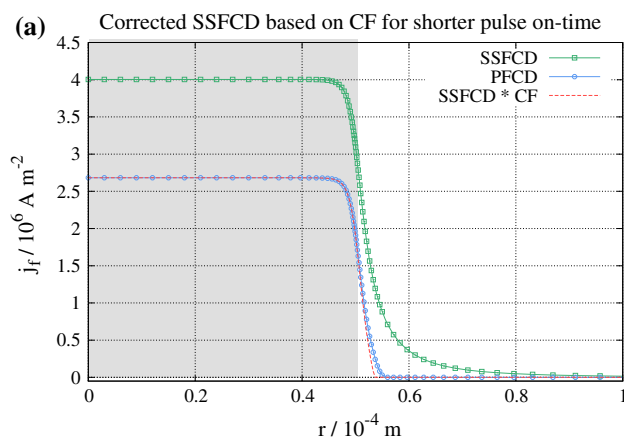


**Fig. 16 a** Time-accurate simulated pulse current density versus steady-state corrected current density. **b** Ratio of simulated pulse current density to steady-state current density versus calculated CF. The pulse  $t_{on} = 20$  ns and  $T = 39$  ns. The grey rectangle marks the cathode limits. The tool sidewalls are insulated

confinement was discussed in detail in previously presented time-accurate simulations [8].

Having explained and discussed the CF for insulated and active sidewalls, the next Section describes how it is used in practice.

### 4.3 Current density correction

The CF was designed to enable fast calculations that would yield the same result as the expensive time-accurate nano-second pulse  $\mu$ ECM simulations [8, 9]. This section provides a comparative analysis between the time-accurate (PFCD) current density distribution and the CF corrected secondary current density distribution (CF-SSFCD), under different conditions.

At first, a stationary numerical simulation (computationally cheap), disregarding the DL capacitance, was performed on the geometry given in Sect. 3.1, with the parameters indicated in Sect. 3.2. The outcome of this procedure represents a steady-state faradaic current

density-SSFCD. A second time-accurate simulation (computationally expensive) including the DL capacitance, was then run by applying pulses with  $t_{\text{on}} = 20$  ns and  $T = 39$  ns. When the system response reached QSS (Sect. 2.2), the pulsed faradaic current density—PFCD—was time averaged, to preserve consistency with Eq. 8.

At this point, by locally applying the time averaged CF to the SSFCD (at every point on the anodic surface) according to Eq. 14, the corrected current density profile could be obtained—SSFCD-CF. Comparing the resulting current density SSFCD-CF to the PFCD showed an almost perfect agreement revealed by Figure 16a. In these pulse conditions, the current density confinement around the cathode was high but with a lower amplitude, leading to lower machining rates. The slight mismatch between the PFCD and the corrected SSFCD-CF thought to be due to numerical accuracy, both in time and space. The mesh discretization in the radius direction would require further refinement, as currently the element length in that region is in the order of  $10^{-6}$  m, which is comparable to the observed misalignment. A linear variation of the CF is assumed within an element. Under the same circumstances, Figure 16b depicts a comparison of the simulated PFCD/SSFCD ratio against the calculated CF. In fact the ratio represents an alternatively computed CF. The almost perfect match between the calculated CF and the PFCD/SSFCD ratio confirms the validity of the CF procedure.

A second example examines the CF behavior for quite different pulse conditions with  $t_{\text{on}} = 100$  ns and  $T = 190$  ns. The results shown in Figure 17a confirm that an accurate match is again obtained, between the SSFCD-CF and the simulated PFCD. Note how well the resulting corrected current density approximates the time-accurate simulation (PFCD), delivering a practically identical amplitude and profile. Figure 17b representing the calculated CF and the ratio PFCD/SSFCD support these results. A calculation for an increased pulse on-time and period, as for example with  $t_{\text{on}} = 1$   $\mu$ s and  $T = 1.9$   $\mu$ s, would align the PFCD to the SSFCD, as the DL loading had occurred sooner than  $t_{\text{on}}/10$ . Note how the CF in Fig. 14 is not confined around the tool anymore under these conditions.

As expected, compared to the pulse conditions presented in Figure 16a, the confinement decreases when the pulse on-time increases. On the other hand the current density is higher, resulting in larger metal removal rates.

The match between the time-accurate and the corrected stationary simulations can be seen as a mutual validation for both the PSS and the previously developed simulation tools [8, 9].

#### 4.4 PSS functional diagram

Enabling rapid calculation times, the PSS can be integrated into versatile ECM simulation software being applied

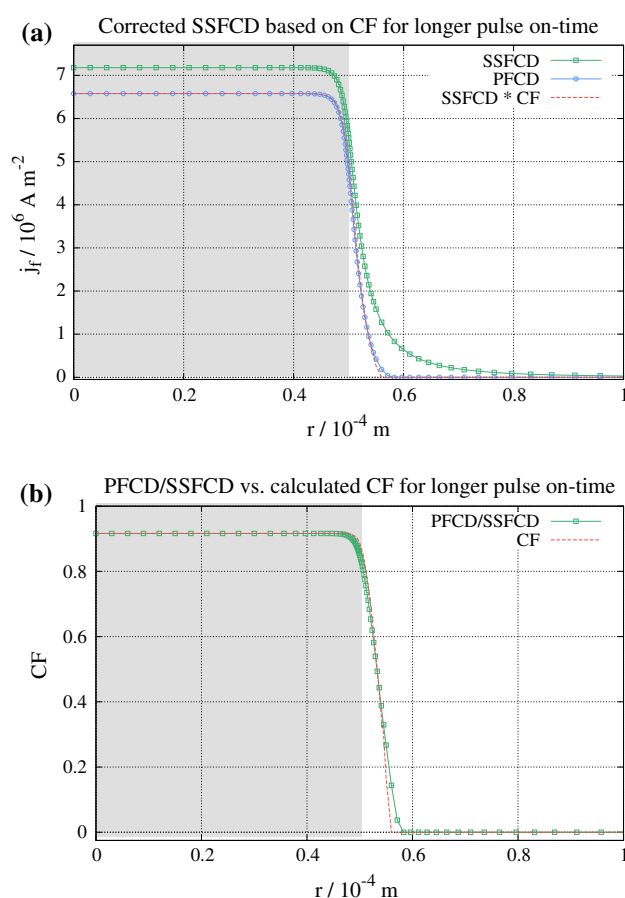


**Fig. 17** **a** Time-accurate simulated pulse current density versus steady-state corrected current density. **b** Ratio of simulated pulse current density to steady-state current density versus calculated CF. The pulse  $t_{\text{on}} = 100$  ns and  $T = 190$  ns. The grey rectangle marks the cathode limits. The tool sidewalls are insulated

today in order to obtain machining profiles in 2D/3D geometries.

The diagram in Figure 18 indicates the four steps involved.

In step 1, the space-dependent resistance (current path length  $l$ ) between the electrodes is calculated. A stationary simulation, based on the PM and disregarding any interface polarization, yields the full distribution range of current density path lengths  $l$ , according to Eq. 13. The inter-electrode path length distribution along the anode is available at the end of this step.

In step 2, the space-dependent CF is computed based on the pulse details, the polarization behavior and the DL properties. The calculation follows the entire sequence given in Sect. 2.3, by solving the system of coefficients that determine the pulse response and the QSS overpotential.

Step 3 computes a stationary secondary current density distribution, including the interface polarization this

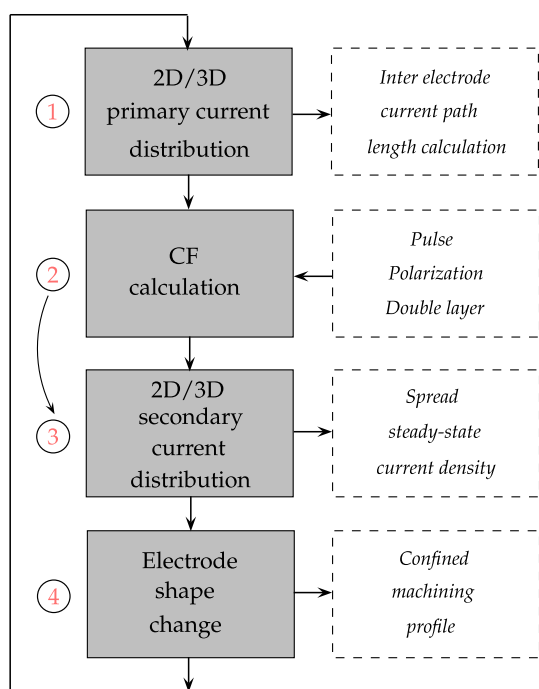


**Fig. 18** Diagram showing the coupled simulation mechanism using the PSS to obtain the final confined workpiece profile. 1–3 stationary simulation, 4 stationary||time-accurate simulation

time. The resulting spread current density distribution is locally altered by the CF, returning a confined distribution, specific to the applied pulse conditions. Note that step 1 and 3 could be integrated as the CF may be calculated based on the secondary current density distribution.

Step 4 includes the calculation of the electrode shape change based on the confined current density distribution and a larger time step followed by a mesh deformation based on any shape change algorithm (e.g. level set method or *Elasticity equations* [9]).

The final outcome of the procedure is a confined machining profile, accomplished by avoiding the time-consuming pulse simulations.

## 5 Conclusions

Nano-second pulse  $\mu$ ECM modelling using full real-time simulations is almost impossible when considering the time steps needed. Even using a hybrid time averaging method [9, 27, 28] proves to be cumbersome when analysing the full time scale range involved [8, 9].

Considering that in many cases the polarization in ECM conditions is linear after a certain threshold potential, assuming that the (average) DL capacitance is constant and finally assuming a constant or averaged electrolyte

conductivity, it is possible to avoid real-time pulse simulations. This is based on the fact that in those conditions the pulsing process essentially behaves as a sequence of two passive linear systems.

It is argued by several numerical simulations that a linear polarization with low resistance does not considerably change the electrical current paths between electrodes in the electrolyte, especially in the zone of interest. The paths can be calculated by solving a Laplace problem. When there is a threshold potential, the system is mainly in either of two modes with fixed current paths: one without faradaic current and one with linear-dependent faradaic current. The presence of a linear capacitance does not influence these modes. By exploiting these important properties, an innovative approach to tackle the pulse simulation process is put forward.

Without significant loss of accuracy, it may be assumed that at pulse time scales the geometry is not changing and that quasi-steady-state pulse conditions are present. This allows, relying on the equivalent circuit along any current line, to pre-calculate the steady-state response over one pulse period. Based on this quasi-steady-state response, a current density CF is introduced that is space-dependent along the workpiece as it depends on the local current density path to the tool. By calculating the CF for a given pulse in advance, and applying it to a non-confined steady-state secondary current density distribution, confined current densities are obtained that depend on the pulse conditions.

The behavior of the CF has been explained and a comparison between the presented approach with full time-accurate pulse simulations shows almost identical numerical results. In fact for most practical applications, the proposed method is fast, sufficiently accurate and easy to integrate into existing ECM simulation tools.

On a broader level it is believed that the CF approach is well-founded and generally applicable. As far as the electrochemical system (the electrolyte and the electrode processes) is sufficiently linear or can be linearised under the working conditions, the presented approach becomes applicable for any imposed periodic potential. Possible usage could be found in pulse plating.

**Acknowledgments** This work has been supported by the European Union Seventh Framework Programme (FP7/2007–2013) under Grant agreement 262072, ECM/Micro ECM for SMEs, Research for the benefit of SMEs FP7-SME-2010-1.

## References

1. Burkert S, Schulze HP, Gmelin T, Leone M (2009) The pulse electrochemical micromachining (pecmm)—specifications of the pulse units. *Int J Mater Form* 2:465–468
2. Datta M, Landolt D (1981) Electrochemical machining under pulsed current conditions. *Electrochim Acta* 26(7):899–907



3. Deconinck D (2012) A temperature dependent multi-ion model for numerical simulation of electrochemical processes-application to electrochemical machining. PhD thesis. Vrije Universiteit, Brussel
4. Deconinck D, Damme SV, Deconinck J (2012a) A temperature dependent multi-ion model for time accurate numerical simulation of the electrochemical machining process. part i: Theoretical basis. *Electrochim Acta* 60:321–328
5. Deconinck D, Damme SV, Deconinck J (2012b) A temperature dependent multi-ion model for time accurate numerical simulation of the electrochemical machining process. part ii: numerical simulation. *Electrochim Acta* 69:120–127
6. Deconinck D, Hoogsteen W, Deconinck J (2013) A temperature dependent multi-ion model for time accurate numerical simulation of the electrochemical machining process. part iii: experimental validation. *Electrochim Acta* 103:161–173
7. Forster R, Schoth A, Menz W (2005) Micro-ecm for production of microsystems with a high aspect ratio. *Microsyst Technol Micro Nanosyst Inf Stor Process Syst* 11:246–249
8. Hotoiu E, Damme SV, Albu C, Deconinck D, Demeter A, Deconinck J (2013) Simulation of nano-second pulsed phenomena in electrochemical micromachining processes effects of the signal and double layer properties. *Electrochim Acta* 93:8–16
9. Hotoiu L, Deconinck J (2013) Time-efficient simulations of nano-pulsed electrochemical micro-machining. *Procedia CIRP* 6:469–474
10. Kenney JA, Hwang GS (2005) Electrochemical machining with ultrashort voltage pulses: modelling of charging dynamics and feature profile evolution. *Nanotechnology* 16:S309–S313
11. Kenney JA, Hwang GS, Shin W (2004) Two-dimensional computational model for electrochemical micromachining with ultrashort voltage pulses. *Appl Phys Lett* 84(19):3774–3776
12. Kirchner V, Xia X, Schuster R (2001) Electrochemical nanostructuring with ultrashort voltage pulses. *Acc Chem Res* 34:371–377
13. Kock M, Kirchner V, Schuster R (2003) Electrochemical micromachining with ultrashort voltage pulses—a versatile method with lithographical precision. *Electrochim Acta* 48:3213–3219
14. Koza JA, Sueptitz R, Uhlemann M, Schultz L, Gebert A (2011) Electrochemical micromachining of a zr-based bulk metallic glass using a micro-tool electrode technique. *Intermetallics* 19(4):437–444
15. Kozak J (2004) Thermal models of pulse electrochemical machining. *Bull Pol Acad Sci: Tech Sci* 52(4):313–320
16. Kozak J, Rajurkar K (1991) Computer simulation of pulse electrochemical machining (pecm). *J Mater Process Technol* 28(1–2):149–157
17. Kozak J, Rajurkar KP, Makkarb Y (2004) Selected problems of micro-electrochemical machining. *J Mater Process Technol* 149:426–431
18. Kozak J, Gulbinowicz D, Gulbinowicz Z (2009) The mathematical modeling and computer simulation of pulse electrochemical micromachining. *AIP Conf Proc* 1127:174–185
19. Lee ES, Baek SY, Cho CR (2005) A study of the characteristics for electrochemical micromachining with ultrashort voltage pulses. *Int J Adv Manufac Technol* 31:762–769
20. Lee G, Jung H, Son J, Nam K, Kwon T, Lim G, Kim YH, Seo J, Lee SW, Yoon DS (2010) Experimental and numerical study of electrochemical nanomachining using an afm cantilever tip. *Nanotechnology* 21:185301
21. Lohrengel MM, Kluppel I, Rosenkranz C, Bettermann H, Schultze JW (2003) Microscopic investigations of electrochemical machining of fe in nano3. *Electrochim Acta* 48:3203–3211
22. Newman J, Thomas-Alyea KE (2004) *Electrochemical systems*, 3rd edn. Wiley, Hoboken, New Jersey
23. Rajurkar K, Zhu D, McGeough J, Kozak J, Silva AD (1999) New developments in electro-chemical machining. *CIRP Ann Manufac Technol* 48(2):567–579
24. Rajurkar KP, Zhy D, Wei B (1998) Minimization of machining allowance in electrochemical machining. *Annals CIRP* 47(1):165–168
25. Schuster R, Kirchner V, Allongue P, Ertl G (2000) Electrochemical micromachining. *Science* 289:98–101
26. Silva AD, Altena H, McGeough J (2000) Precision ecm by process characteristic modelling. *CIRP Ann Manufac Technol* 49(1):151–155
27. Smets N (2009) Towards time-efficient simulations in pulse electrochemical machining. PhD Thesis. Vrije Universiteit, Brussel
28. Smets N, Damme SV, Wilde DD, Weyns G, Deconinck J (2007) Time averaged temperature calculations in pulse electrochemical machining. part i: theoretical basis. *J Appl Electrochem* 37:1345–1355
29. Smets N, Damme SV, Wilde DD, Weyns G, Deconinck J (2008) Time averaged temperature calculations in pulse electrochemical machining. part ii: numerical simulations. *J Appl Electrochem* 38:551–560